Received: 14 May 2023 | Revised: 29 July 2023 | Accepted: 5 August 2023

DOI: 10.1111/ffe.14132

ORIGINAL ARTICLE

FFEMS Fatigue & Fracture of Engineering Materials & Structures WILEY

Estimating the intrinsic dissipation using the second-harmonic temperature signal in the tension–tension fatigue

Mauro Ricotta | **Giovanni Meneghetti**

Department of Industrial Engineering, University of Padua, Padova, Italy

Correspondence
Giovanni Meneghetti, Department of Industrial Engineering, University of Padua, via Venezia, 1-35131 Padova, Italy.
Email: giovanni.meneghetti@unipd.it

Funding information
European Union, Grant/Award Number: 101058179

Abstract

The intrinsic dissipation experienced by a metal under tension–tension fatigue is linked to the second-harmonic temperature signal obtained from Fourier analysis. According to the proposed model, self-heating due to intrinsic dissipation spreads out into all harmonics of the temperature signal, including that modulated at the same frequency as the applied load, which primarily captures the thermoelastic effect. Furthermore, the model is adapted to estimate the intrinsic dissipation starting from the second-harmonic temperature if the command signal generated by the closed-loop digital controller of the fatigue test machine is not a pure sine wave modulated at the desired load test frequency but contains high-order harmonics. Finally, the theoretical model is applied to measure the intrinsic dissipation during stepwise fatigue tests on plain specimens made of C45 normalized steel, and the results obtained are validated using a previously well-established approach.

KEYWORDS

energy approaches, energy dissipation, fatigue, thermal methods

Highlights

- A model is defined for estimating the intrinsic dissipation in tension–tension fatigue.
- The model requires the range of the second-harmonic temperature of the material.
- The model cleans high-order harmonics generated by the controller of the test machine.
- The model is successfully validated through fatigue tests on C45 normalized steel.

1 | INTRODUCTION

The fatigue of metals can be addressed from an energy point of view. The mechanical energy provided by the external loads is split by the material into two parts,[1] including the internal energy, which is partially responsible for fatigue damage accumulation and final failure, and the heat dissipated to the surroundings, which determines the material's self-heating. Therefore, the material temperature is envisaged to be a useful parameter for the development of *temperature-based* approaches for investigating the fatigue behavior and limit of metals,[2–8] to perform thermoelastic analyses at the tip of a propagating fatigue crack,[9–13] fatigue life assessment and identification of fatigue damage evolution laws,[14–16] and evaluations of cumulative damage for variable amplitude and multiaxial fatigue loadings.[17–21] Notably, some authors have proposed using the second-harmonic temperature signal[22,23] or thermoelastic phase analysis[24] to rapidly evaluate the material fatigue limit.

The stationary material temperature achieved during a constant amplitude fatigue test with a given load test frequency is correlated to the thermal energy released to the surroundings by a unit volume of material per cycle ($\overline{Q}$).[25] $\overline{Q}$ has been identified as the intrinsic dissipation $\overline{Q}_p$[26] and proved successful as an *energy-based* fatigue damage index to correlate geometrical effects in fatigue,[27–30] to estimate the fatigue limit,[31] and to synthesize the multiaxial fatigue behavior.[32] In addition to intrinsic dissipation,[33,34] similar *energy-based* approaches for fatigue assessment are based on the hysteresis energy per cycle[1,35,36] and on entropy evaluation.[37,38]

By focusing on fully reversed ($R = -1$) fatigue tests with an elastic–plastic material, Enke[39] noted that the material temperature pulses as a result of two different phenomena—the reversible thermoelastic (T_{the}) and irreversible plastic dissipation (T_p) temperatures—where the latter pulses at twice the fundamental frequency of the reversible thermoelastic effect, which equals the load test frequency. In this context, Bar et al.[40] showed that T_p is not fully captured by considering only the second harmonic of the temperature signal ΔT_2, even though the second harmonic retains the main information.[40,41] This phenomenon is why several evaluations of the intrinsic dissipation, $\overline{Q}_p$, in tension–compression fatigue tests start from the range of the second-harmonic temperature signal ΔT_2.[40–44] Recently, De Finis et al.[44] extended the analysis to the case of tension–tension ($R > 0$) fatigue and investigated the relationship between mechanical energy and heat dissipation; the outcome of the investigation is an empirical linear correlation between the second harmonic of the mechanical energy rate and the second harmonic of the heat dissipation rate.

Considering the situation of tension–compression ($R = -1$) fatigue, under the hypotheses of (i) zero-dimensional thermomechanical material model, (ii) plastic strain energy rate, $\dot{W}$, totally converted into heat, $\dot{Q}$, and (iii) elastic–perfectly plastic material behavior or elastic–plastic obeying a Ramberg–Osgood law, the authors developed an analytical framework to evaluate the intrinsic dissipation $\overline{Q}_p$ starting from the range of the second-harmonic temperature signal ΔT_2, which is evaluated by the Fourier analysis of the material temperature.[45] When a material obeying a Ramberg–Osgood law was considered, $\overline{Q}_p$ is linked to ΔT_2 through a parameter (β) that depends on the cyclic strain hardening exponent n' of the material.[45] Afterwards, the model was validated against temperature maps recorded during axial tension–compression, load-controlled, stepwise fatigue tests of cold-drawn AISI 304L bars[46]; in particular, the $\overline{Q}_p$ values are successfully compared with those measured using a previously validated experimental technique proposed by one of the authors.[25]

Recently, the authors tried to extend the analytical model to R ratios of at least zero ($R \geq 0$)[47] and removed the assumption that $\dot{W}$ is totally converted into $\dot{Q}$, while retaining the zero-dimensional thermomechanical material model and the Ramberg–Osgood material law. $\overline{Q}_p$ depends on the range of the second-harmonic temperature signal through the β parameter, and it has a different analytical dependence on the cyclic strain hardening exponent n' relative to the previous case $R = -1$, as seen in the next paragraph.

Prior to the investigation,[47] Shiozawa et al.[48] analyzed the correlation between the second-harmonic temperature signal and the intrinsic dissipation, aiming to rapidly evaluate the material fatigue limit; the researchers noted that the closed-loop digital controller of the fatigue test machine may introduce harmonics in addition to that modulated at the load test frequency. In more detail, the scholars noticed that these spurious effects can be corrected using a modified lock-in infrared technique based on the measured phase difference between the second-harmonic temperature signal and the load signal. Later, Cappello et al.[49] analyzed the discrete Fourier transform (DFT) of the load cell signal of the fatigue test machine and found high-order harmonics superimposed on the fundamental sine wave corresponding to the applied load test frequency. Hence, the second-harmonic load causes a thermoelastic response at twice the applied load test frequency that overlaps with the second-harmonic temperature that is strictly related to the intrinsic dissipation.

Additionally, high-order harmonics are more frequently present for tension–tension fatigue tests than for fully reversed tension–compression fatigue tests, and a simple analytical expression is proposed to extract the second-harmonic temperature signal strictly related to the intrinsic dissipation.[49]

In this paper, after recalling the theoretical background relevant to R ratios of at least zero, the theoretical model is employed to estimate the intrinsic dissipation starting from the second-harmonic temperature. The model considers the unique features of (i) the self-heating phenomenon, which spreads the effects of dissipation into all temperature harmonics, including that modulated at the load test frequency, and (ii) the experimental test equipment, where the closed-loop digital controller of the fatigue test machines may introduce high-order and fundamental harmonics. Compared to the previous preliminary study,[47] the present investigation proposes the following advances:

- New equations are proposed to evaluate the second-harmonic temperature range associated with the intrinsic dissipation when the command signal generated by the closed-loop digital controller of the fatigue test machine contains high-order harmonics superimposed on the fundamental (first-order, pure sinusoidal) one;
- A large number of new experimental data, consisting of 56 measurements of the intrinsic dissipation;
- The energy conversion ratio, namely, the ratio between the intrinsic dissipation and the plastic strain energy density per cycle, is evaluated in tension–tension fatigue for different applied stress amplitudes.

Finally, the intrinsic dissipation $\overline{Q}_p$ is evaluated in stepwise fatigue tests on plain specimens, and the values obtained from the second-harmonic temperature signal are compared with those evaluated according to a well-established approach based on the cooling gradient of the material measured after stopping the fatigue test.[25] The paper is concluded with a discussion regarding the two approaches.

2 | THEORETICAL BACKGROUND

The energy balance equation developed according to continuum mechanics[50] can be written in terms of the specific power as follows,[26] where the dot symbol indicates the time derivative:

$$\rho c\dot{T} - \dot{Q} = \dot{Q}_p + \dot{Q}_{the} + \dot{v}_e \quad (1)$$

where $\dot{Q}_{the}$ and $\dot{Q}_p$ are the thermoelastic energy and the intrinsic dissipation rates, respectively, and $\dot{v}_e$ is the thermal energy rate extracted from or supplied to the material by external sources. Equation (1) is true after certain simplification hypotheses,[26,45] which are satisfied in conventional fatigue test conditions. The intrinsic dissipation is defined as follows[50]:

$$\dot{Q}_p = \dot{W} - \dot{E}_s \quad (2)$$

where $\dot{W}$ and $\dot{E}_s$ are the plastic strain and stored energy rates, respectively.[51,52]

In the experimental conditions analyzed in the present investigation, $\dot{v}_e$ equals zero; moreover, the thermoelastic heat source is a reversible exchange between mechanical and thermal energies[53,54]; therefore, it vanishes in Equation (1), which is rewritten in terms of average power quantities over one loading cycle as follows:

$$\rho c\dot{\overline{T}} - \dot{\overline{Q}} = \dot{\overline{Q}}_p \quad (3)$$

$\overline{T}(t)$ stabilizes at a certain period following the start of a fatigue test when thermal equilibrium is achieved between intrinsic dissipation and heat exchange with the surroundings by conduction, convection, and radiation.[5,7,17,21,25,38] Under such circumstances, $\dot{\overline{T}}$ becomes null, and Equation (3) simplifies to the following equation[25]:

$$\dot{\overline{Q}} = -\dot{\overline{Q}}_p \quad (4)$$

2.1 | Cooling gradient approach

According to the *cooling gradient approach*,[25,45] the intrinsic dissipation $\dot{\overline{Q}}_p$ is estimated by measuring the cooling gradient immediately after the fatigue test is stopped at $t = t^*$ (Figure 1). While $\dot{\overline{Q}}_p$ becomes zero at $t = t^{*+}$, the heat exchanged with the surroundings $\dot{\overline{Q}}$ does not change before or immediately after t* because the temperature field is constant through t* (i.e., $T|_{(t*)^-} = T|_{(t*)^+}$). Accordingly, Equation (3) must be considered immediately after t* (i.e., $t = t^{*+}$), leading to the following equation:

$$\dot{\overline{Q}} = \rho \cdot c \cdot \dot{T}\big|_{t=(t*)^+} \quad (5)$$

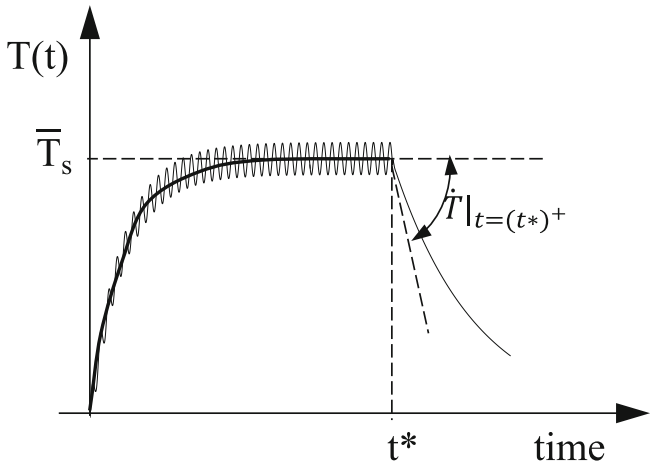

FIGURE 1 Cooling gradient approach for estimating the intrinsic dissipation.

Eventually, $\overline{Q}$ can be evaluated by dividing Equation (5) by the load test frequency f_L[25]:

$$\overline{Q} = \frac{\rho \cdot c \cdot \dot{T}|_{t=(t*)^+}}{f_L} \tag{6}$$

2.2 | Second harmonic approach

The cooling gradient approach, originally formalized in Meneghetti,[25] has been subsequently applied in several investigations,[27–32,37,38] and it is used in the present research to validate the approach based on the second-harmonic temperature signal; this technique is referred to as the *second harmonic approach*, and it is summarized as follows. According to the original formulation,[45] completely reversed ($R = -1$) elastic–plastic fatigue tests are considered, and the correlation between intrinsic dissipation $\overline{Q}_p$ and the range of the second-harmonic temperature signal ΔT_2 is expressed as follows:

$$\overline{Q}_p = \rho \cdot c \cdot 2 \cdot \Delta T_2 \cdot \beta \tag{7}$$

where β is a parameter that must be determined, and the coefficient 2 considers that two temperature shots occur per cycle, one of which is caused by tensile strains and the other of which is caused by compressive plastic strains over one loading cycle.[39,40,42] To evaluate the β parameter for tension–compression ($R = -1$) fatigue, a simplified zero-dimensional thermomechanical theoretical model is considered, where the intrinsic dissipation is known; after solving the governing differential equation (Equation (1)), the temperature versus time is calculated. Then, Fourier analysis of the temperature is performed to first obtain ΔT_2 and then obtain β using Equation (7). As mentioned in Section 1, a simplifying hypothesis of the theoretical model is that $\dot{W}$ is fully converted into $\dot{Q}_p$, therefore the stored energy rate $\dot{E}_s$ is negligible, which is consistent with the literature, particularly for tension–compression ($R = -1$) fatigue.[27,31,55–58] Second, in the framework of a zero-dimensional thermomechanical material model, heat extraction from the material is activated using a heat sink $\dot{v}_e$, such that $\dot{v}_e = -\overline{W} \cdot f_L$, to let the material temperature achieve stationarity (under real laboratory testing conditions, the heat due to intrinsic dissipation is removed from the material by conduction, convection, and radiation). Even though the hypothesis $\dot{W} \cong \dot{Q}_p$ is used,[45] if $\dot{Q}_p$ is a fraction of $\dot{W}$, then β is unchanged according to the adopted theoretical model.

Regarding R ratios of at least zero ($R \geq 0$),[47] to the best of the authors' knowledge, there are no experimental data supporting the general assumption $\dot{W} \cong \dot{Q}_p$, which is consequently removed in the present investigation; conversely, the zero-dimensional thermomechanical model and the heat extraction mechanism using the heat sink are retained. Accordingly, an energy conversion ratio Ψ is defined as follows:

$$\Psi = \frac{\dot{Q}_p}{\dot{W}} \rightarrow = 1 - \frac{\dot{E}_s}{\dot{W}} \tag{8}$$

According to Equation (7), coefficient 2 is maintained because in pulsating tension or tension–tension ($R \geq 0$) fatigue, the intrinsic dissipation associated with plastic work is generally active during the loading and unloading phases:

$$\overline{\Psi} \cdot \overline{W} = \overline{Q}_p \rightarrow = \rho \cdot c \cdot 2 \cdot \Delta T_2 \cdot \beta \tag{9}$$

The energy balance Equation (1), which is written in terms of power quantities, becomes the following equation:

$$\rho c \dot{T}_p + \rho c \dot{T}_{the} + \rho c \dot{T}_{sink} = \Psi \dot{W} + \dot{Q}_{the} - \overline{\Psi} \cdot \overline{W} \cdot f_L \tag{10}$$

The solution of Equation (10) is determined assuming (i) $\Psi = \overline{\Psi}$, (ii) an elastic–plastic material obeying Ramberg–Osgood law, and (iii) a tension–tension, force-controlled fatigue test with a sinusoidal load causing the

stress amplitude σ_a and mean stress σ_m as $\sigma(t)=\sigma_a\cdot\sin(\omega_L t)+\sigma_m$. Figure 2A shows the stabilized hysteresis loop in a typical tension–tension fatigue test and the reference system at its lower tip (Figure 2A). Now it is convenient to solve Equation (10) by taking the stress function as follows:

$$\Delta\sigma^*(t)=\sigma_a[1-\cos(\omega_L t)]. \tag{11}$$

The first term on the right-hand side of Equation (10) is the rate of plastic strain energy, and it can be expressed as follows[47]:

$$\dot{W}(t)=\dot{W}_L(t)\cdot R_L(t)+\dot{W}_U(t)\cdot R_U(t) \tag{12}$$

where referring to Figure 2B, $\dot{W}_L(t)$ is the rate of the plastic strain energy for $0\le t\le \widehat{T}/2$:

$$\dot{W}_L(t)=\frac{\omega_L}{n'}\cdot\frac{\sigma_a^{\frac{1}{n'}+1}}{2^{\frac{1}{n'}-1}\cdot K'^{\frac{1}{n'}}}\cdot\sin(\omega_L t)\cdot\left[\frac{2R}{1-R}+1-\cos(\omega_L t)\right]\cdot[(1-\cos(\omega_L t)]^{\frac{1}{n'}-1} \tag{13a}$$

$\dot{W}_U(t)$ is the plastic strain energy rate for $\widehat{T}/2\le t\le\widehat{T}$:

$$\dot{W}_U(t)=-\frac{\omega_L}{n'}\cdot\frac{\sigma_a^{\frac{1}{n'}+1}}{2^{\frac{1}{n'}-1}\cdot K'^{\frac{1}{n'}}}\cdot\sin(\omega_L t)\cdot\left[\frac{2R}{1-R}+1-\cos(\omega_L t)\right]\cdot[(1+\cos(\omega_L t)]^{\frac{1}{n'}-1} \tag{13b}$$

where $R_L(t)$ and $R_U(t)$ are dedicated rectangular waves. More precisely, the former value is equal to one in the $0\le t\le\widehat{T}/2$ time window and zero elsewhere, while the latter equals one for $\widehat{T}/2\le t\le\widehat{T}$ and zero elsewhere (Figure 2C). For the convenience of the reader, the definitions of $R_L(t)$ and $R_U(t)$ are Equations (14a) and (14b), respectively:

$$R_L(t)=\frac{1}{2}+\frac{2}{\pi}\sum_{j=1}^{\infty}\frac{\sin(j\cdot\pi/2)}{j}\cdot\cos\left\{j\cdot\omega_L\left[t-\frac{\widehat{T}}{4}\right]\right\} \tag{14a}$$

$$R_U(t)=\frac{1}{2}+\frac{2}{\pi}\sum_{j=1}^{\infty}\frac{\sin(j\cdot\pi/2)}{j}\cdot\cos\left\{j\cdot\omega_L\left[t-\frac{1}{2}\left(\frac{\widehat{T}}{2}+\widehat{T}\right)\right]\right\} \tag{14b}$$

The three contributions to the material temperature appearing in Equation (10) can be evaluated as follows. The thermoelastic temperature $\Delta T_{the}(t)$ can be evaluated from the corresponding thermoelastic heat source $\dot{Q}_{the}$[59,60]:

$$\Delta T_{the}(t)=-\left(\frac{\alpha}{\rho\cdot c}\right)\cdot\Delta\sigma^*(t)\cdot T_0 \tag{15}$$

where T_0 is the material temperature when $\Delta\sigma^*(0)=0$, that is, $\sigma=\sigma_{min}$.

The dissipation temperature $\Delta T_p(t)$ associated with the plastic dissipation is calculated as follows:

$$\begin{aligned}\Delta T_p(t)&=\frac{1}{\rho\cdot c}\int_0^t\Psi\dot{W}(t)\cdot dt=\\&=\frac{\overline{\Psi}}{\rho\cdot c}\frac{\sigma_a^{\frac{1}{n'}+1}}{2^{\frac{1}{n'}-1}\cdot(n'+1)\cdot K'^{\frac{1}{n'}}}\left\{\frac{\cos(\omega_L t)(R-1)+R(2n'+1)+1}{1-R}\cdot[1-\cos(\omega_L t)]^{\frac{1}{n'}}\cdot R_L(t)+\right.\\&\left.+\left[\frac{[(1+\cos(\omega_L t)]^{\frac{1}{n'}}\cdot\cos(\omega_L t)\text{-}R(1+\cos(\omega_L t))\text{-}1\text{-}2\cdot n'}{R-1}+\frac{2^{\frac{1}{n'}+1}}{1\text{-}R}\cdot(1+R\cdot n')\right]\cdot R_U(t)\right\}\end{aligned} \tag{16}$$

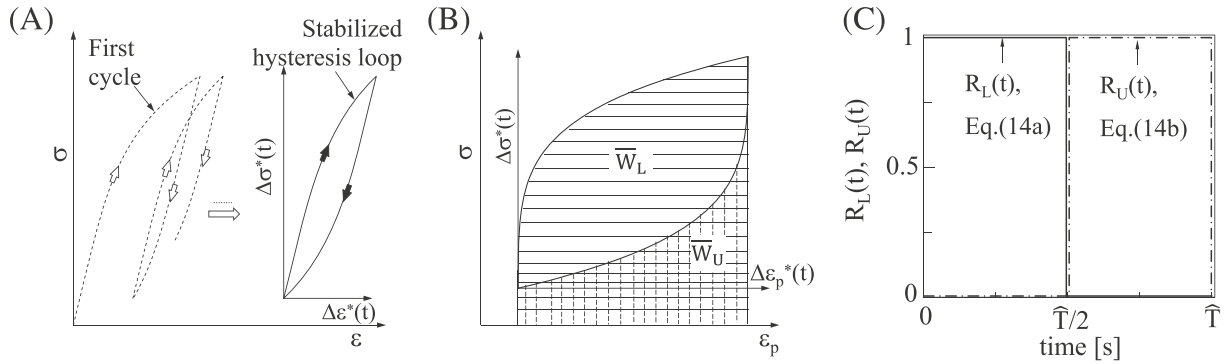

FIGURE 2 (A) Stabilized hysteresis loop for an elastic–plastic material obeying a Ramberg–Osgood law, (B) plastic strain energy densities in one loading cycle, and (C) rectangular wave functions $R_L(t)$ and $R_U(t)$.

Finally, the heat sink temperature $\Delta T_{sink}(t)$ is as follows[47]:

$$\Delta T_{sink}(t) = -\frac{\overline{\Psi}\cdot\overline{W}\cdot f_L}{\rho\cdot c}\cdot t \tag{17}$$

Thus, by summing the three contributions of Equations (15), (16), and (17), the solution of Equation (10) is as follows:

$$\Delta T(t) = \Delta T_p(t) + \Delta T_{the}(t) + \Delta T_{sink}(t) \tag{18}$$

Equation (18) refers to the stress function $\Delta\sigma^*(t)$, which is zeroed at the lower tip of the hysteresis loop. To refer to the solution of the stress function $\sigma(t)$ and not to $\Delta\sigma^*(t)$, $\Delta T(t)$ must be shifted by a factor of $\frac{\widehat{T}}{4}$; then, the temperature of the unstressed state is referenced:

$$T(t) = \Delta T\left(t+\frac{\widehat{T}}{4}\right) + T_0 \tag{19}$$

Equation (19) provides the stationary material temperature T(t) according to the theoretical model Equation (10). Since the equation is periodic, it can be written using a Fourier series as follows:

$$T(t) = \overline{T}_s + \sum\nolimits_{k=1}^{\infty}[A_k\cdot\cos(k\omega_L t) + B_k\cdot\sin(k\omega_L t)] \tag{20}$$

where $\omega_L = 2\pi\cdot f_L$ and $\widehat{T} = 2\pi/\omega_L = \frac{1}{f_L}$.

$$A_k = \frac{2}{\widehat{T}}\int_0^{\widehat{T}} T(t)\cdot\cos(k\cdot\omega_L\cdot t)dt \text{ for } k>0 \tag{21a}$$

$$B_k = \frac{2}{\widehat{T}}\int_0^{\widehat{T}} T(t)\cdot\sin(k\cdot\omega_L\cdot t)dt \text{ for } k\geq 0 \tag{21b}$$

$$\overline{T}_s = \frac{A_0}{2} = \frac{1}{\widehat{T}}\int_0^{\widehat{T}} T(t)dt \tag{21c}$$

The ranges of the first- and second-harmonic temperatures are displayed in Equations (22a) and (22b), respectively, as follows:

$$\Delta T_1 = 2\cdot\sqrt{A_1^2+B_1^2} \tag{22a}$$

$$\Delta T_2 = 2\cdot\sqrt{A_2^2+B_2^2} \tag{22b}$$

The stationary temperature (Equation (19)) and its Fourier analysis are illustrated with an example in the next paragraph.

Finally, β is calculated using Equation (9). According to previous investigations, β depends only on n′, regardless of the R (for $R\geq 0$) and Ψ values; however, β for $R\geq 0$ is different from that calculated for $R=-1$,[45] as reported in Figure 3[47]:

$$\beta = 0.566\cdot n'^2 + 2.671\cdot n' + 1.572 \quad (R\geq 0) \tag{23}$$

3 | THEORETICAL STATIONARY TEMPERATURE AND FOURIER ANALYSIS ACCORDING TO THE SECOND HARMONIC APPROACH ($R \geq 0$)

Equation (19) is plotted in Figure 4A,C for $R=0$ and $R=0.5$, respectively, with the first, second, third, and fourth harmonic waves of T(t) evaluated according to Equation (21). Additionally, the applied stress function

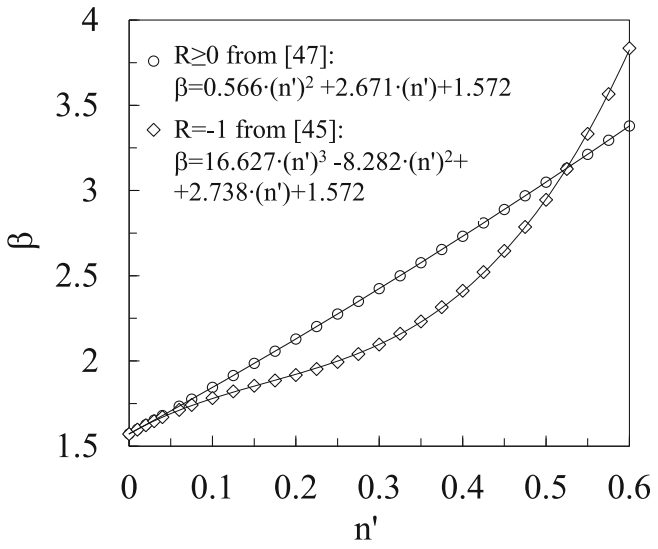

FIGURE 3 Trends of the β parameter versus the cyclic strain hardening exponent.

σ(t) and the stationary dissipation temperature $T_{ps}(t)$ are reported in the same figures. In the adopted theoretical model, $T_{ps}(t)$ is defined when the stabilized temperature $\overline{T}_s$ is achieved, according to Figure 1. In the stabilized regime, a thermal equilibrium exists between the self-heating phenomenon caused by the intrinsic dissipation and the heat extraction from the material to the surroundings. $T_{ps}(t)$ represents the thermal equilibrium between the self-heating phenomenon caused by the intrinsic dissipation (captured by the continuously increasing dissipation temperature Equation (16)) and the heat extraction from the material to the surroundings (captured by the heat sink temperature Equation (17)). In real experimental tests, the higher the stabilized dissipation temperature $\overline{T}_{ps}$, the more intense the intrinsic dissipation phenomenon is, and the less efficient the heat removal from the material to the surroundings

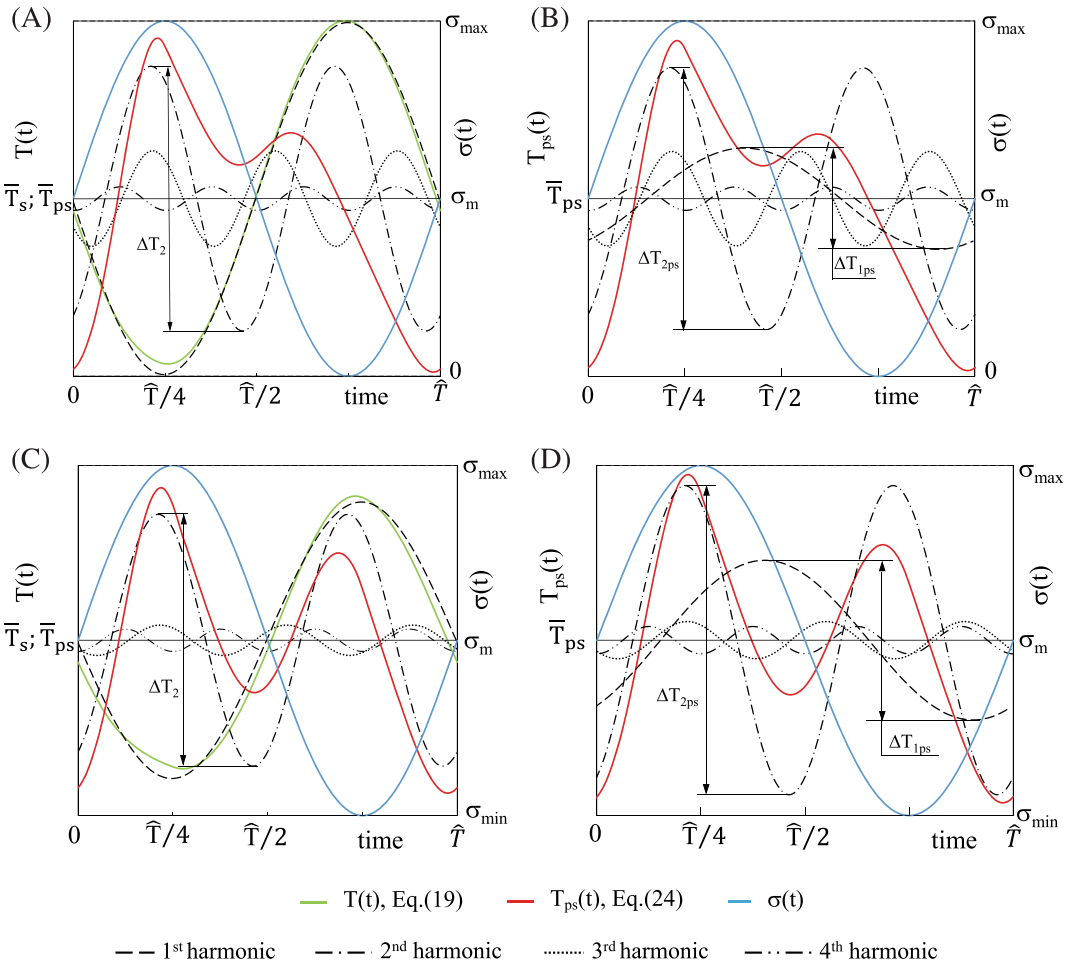

FIGURE 4 Stationary T(t) and dissipation $T_{ps}(t)$ temperatures of the material over one loading cycle for (A), (B) R = 0 and (C), (D) R = 0.5 evaluated with n′ = 0.4 and Ψ = 0.45. The figures are created according to the σ–ε coordinate system reported in Figure 2. (A) $T_{ps}(t)$ magnified 13 times, and the second, third, and fourth harmonics of T(t) magnified 52 times; (B) all four harmonics of $T_{ps}(t)$ magnified four times; (C) $T_{ps}(t)$ magnified eight times, and the second, third, and fourth harmonics of T(t) magnified 21 times; and (D) all four harmonics of $T_{ps}(t)$ magnified three times. [Colour figure can be viewed at wileyonlinelibrary.com]

(by conduction, convection, and radiation) is. As a second remark, it should be noted that $\overline{T}_{ps} = \overline{T}_s$.

Since, according to the theoretical model, $T_{ps}(t)$ is the net result of the phenomena captured by Equations (16) and (17), it can be written:

$$T_{ps}(t) = \Delta T_p\left(t + \frac{\widehat{T}}{4}\right) + \Delta T_{sink}\left(t + \frac{\widehat{T}}{4}\right) + T_0 \qquad (24a)$$

alternatively, Equations (18) and (19) yield the following equation:

$$T_{ps}(t) = T(t) - \Delta T_{the}\left(t + \frac{\widehat{T}}{4}\right) \qquad (24b)$$

Having determined the stationary dissipation temperature using the analytical model, the influence of the load ratio R can be investigated by means of the Fourier analysis Equation (21) applied to the $T_{ps}(t)$ function (Equation (24)); the results are plotted in Figure 4B (R = 0) and Figure 4D (R = 0.5).

Figure 4A,C shows that $T_{ps}(t)$ is not a sinusoidal wave, and a similar behavior is observed for R = −1.[45] Moreover, unlike tension–compression fatigue (R = −1), Figure 4B,D shows that for R ≥ 0, the stationary dissipation temperature $T_{ps}(t)$ spreads out into all harmonics, starting from the first and involving all terms of the Fourier series, including the odd ones (one, third, fifth, etc.), which are not involved when R = −1.[45] In fact, in tension–compression (zero-mean stress, R = −1) fatigue, the intrinsic dissipation in a fatigue cycle is equally divided between the loading and unloading phases. Therefore, the stationary dissipation temperature has exactly the same trend (and values) in the first half cycle (the loading phase) and in the second half cycle (the unloading phase). That is why only the even coefficients of the Fourier series are different from zero, while the odd terms are null.[45] Opposite to this situation, under pulsating tension and tension–tension fatigue (R ≥ 0), the intrinsic dissipation in a fatigue cycle is not equally divided between the loading and unloading phases. This phenomenon can be easily appreciated in Figure 2B, where the plastic strain energy density is greater in the loading phase than in the unloading phase. Therefore, the stationary dissipation temperature $T_{ps}(t)$ trend (and values) during the loading phase differs from those relevant to the unloading phase, and this is evident in Figure 4A,C of the present paper. Such asymmetry of $T_{ps}(t)$ during the loading and unloading phases makes the intrinsic dissipation spread out into all harmonics of the temperature signal, including the fundamental one modulated at the load test frequency, which primarily captures the thermoelastic effect. Interestingly, the results of the analyses reported in Figure 4A,B for R = 0 and in Figure 4C,D for R = 0.5 highlight that ΔT_2 equals ΔT_{2ps}; that is, the second-harmonic analysis of the temperature returns the same result as the second-harmonic analysis of the stationary dissipation temperature. The differences between ΔT_2 and ΔT_{2ps} that are appreciable in the figures simply depend on the different scales on the Y-axis. In general, all harmonics of T(t) and $T_{ps}(t)$ are the same starting from the second harmonic onwards, and the thermoelastic temperature is fully captured by the first harmonic of T(t), at least for a pure sinusoidal load wave, such as in the present theoretical analysis.

Figure 5 reports the $\Delta T_{1ps}/\Delta T_2$ ratio versus R for different n′ values and highlights that the ratio decreases when R and n′ increase. The $\Delta T_{1ps}/\Delta T_2$ ratio does not depend on σ_a, K′, and Ψ. Moreover, the figure shows that ΔT_{1ps} is greater than ΔT_2 for lower R and n′ values; therefore, in tension–tension fatigue, ΔT_2 may no longer convey most of the information.[44]

Thanks to the assumption of a Ramberg–Osgood description of the branches of the hysteresis loop (Figure 2), comparing the plastic strain energy density $\overline{W}$ with the hysteresis energy density, $\overline{W}_{hyst}$, is valuable. $\overline{W}$ can be evaluated by integrating Equation (12) over one loading cycle:

$$\overline{W} = \int_0^{\widehat{T}} \dot{W}(t)dt = \frac{1+R}{1-R} \cdot \frac{4 \cdot \sigma_a^{\frac{1}{n'}+1}}{K'^{\frac{1}{n'}}} \qquad (25)$$

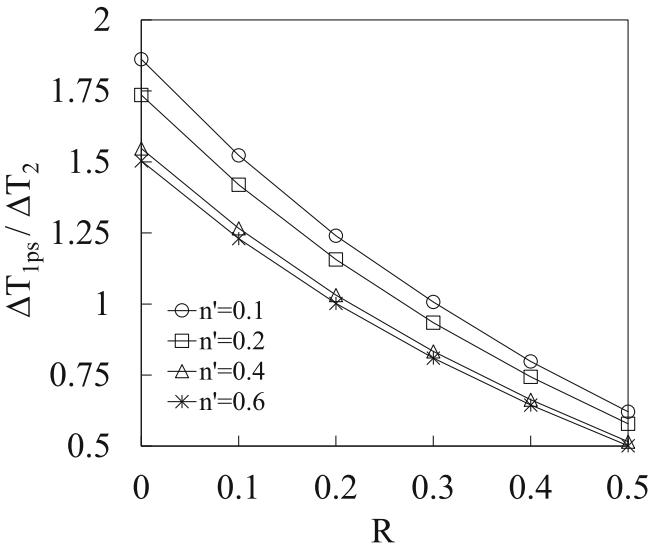

FIGURE 5 ΔT_{1ps} to ΔT_2 ratio versus R calculated for different n′ values.

Equation (25) is valid for $R \geq 0$, while the expression valid for $R = -1$ has been derived elsewhere.[45]

$\overline{W}_{hyst}$ can be evaluated according to Halford[36]:

$$\overline{W}_{hyst} = \frac{1-n'}{1+n'} \cdot \frac{4 \cdot \sigma_a^{\frac{n'}{7}+1}}{K'^{\frac{1}{n'}}}. \quad (26)$$

Therefore, the $\overline{W}_{hyst}/\overline{W}$ ratio is as follows:

$$\frac{\overline{W}_{hyst}}{\overline{W}} = \frac{1-n'}{1+n'} \cdot \frac{1-R}{1+R} \quad (27)$$

Equation (27) shows that the $\overline{W}_{hyst}/\overline{W}$ ratio depends on n' and R, and it is plotted in Figure 6A,B. Figure 6A reports Equation (27) for the $R = -1$ case.[45]

Figure 7A,B shows the trends of ΔT_{1ps} and ΔT_2 versus R for an exemplary set of material parameters ($n' = 0.2$, $K' = 700$ MPa, $\rho = 7850$ kg/m^3, $c = 486$ J/(kg·K), and $\Psi = \overline{\Psi} \rightarrow = 0.75$) and testing conditions ($f_L = 1$ Hz, $\sigma_a = 310$ MPa, or $\overline{W} = 21$ MJ/(m^3·cycle)). In particular, Figure 7A assumes a constant applied stress amplitude $\sigma_a = 310$ MPa, while Figure 7B assumes a constant plastic strain energy per cycle $\overline{W} = 21$ MJ/(m^3·cycle), which suggests a constant intrinsic dissipation $\overline{Q}_p$ according to Equation (9) ($\overline{Q}_p = \overline{\Psi} \cdot \overline{W} = 0.75 \cdot 21 = 15.75$ MJ/(m^3·cycle)). Figure 7A shows that ΔT_{1ps} assumes a constant value regardless of R, while ΔT_2 increases when R increases because $\overline{W}$ and then $\overline{Q}_p$ increase according to Equation (25). An opposite scenario is reported when $\overline{W}$ is constant (Figure 7B); ΔT_2 remains constant ($\Delta T_2 = 0.97$ K), independent of R, while ΔT_{1ps} decreases, following the progressively decreasing σ_a that maintains $\overline{W}$, according to Equation (25). Considering this information, the range of the second-harmonic temperature ΔT_2 is correlated to the intrinsic dissipation $\overline{Q}_p$. However, the use of the β parameter (Equation 9) is needed to quantitatively evaluate the intrinsic dissipation starting from the range of the second-harmonic temperature. By using Equation (23) with $n' = 0.2$, it is found that $\beta = 2.129$ and $\overline{Q}_p = 15.75$ MJ/(m^3·cycle) from Equation (9).

4 | MATERIAL, SPECIMENS' GEOMETRY, AND TEST METHOD

The experimental equipment and testing protocol described in this section were applied in a preliminary investigation[47] using a single specimen. Figure 8A shows the geometry of the plain specimens adopted to perform stepwise tension–tension fatigue tests, imposing a nominal load ratio of $R = 0.1$. Samples were machined from

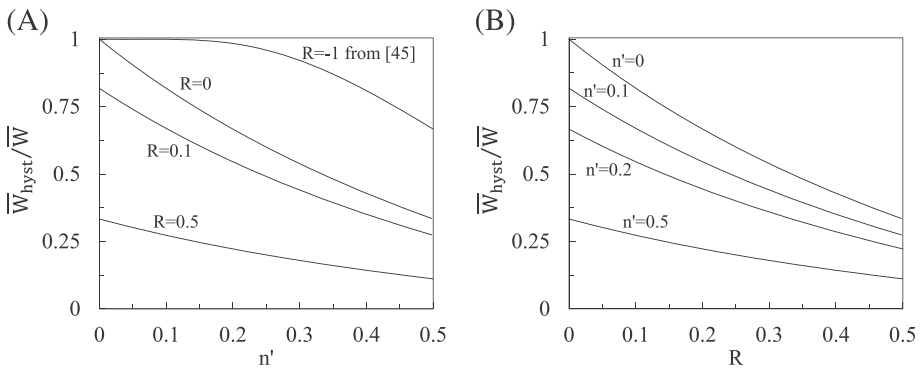

FIGURE 6 Ratio between hysteresis and plastic strain energy densities per cycle (Equation (27)) (A) versus the cyclic hardening exponent, n' and (B) versus the load ratio, R.

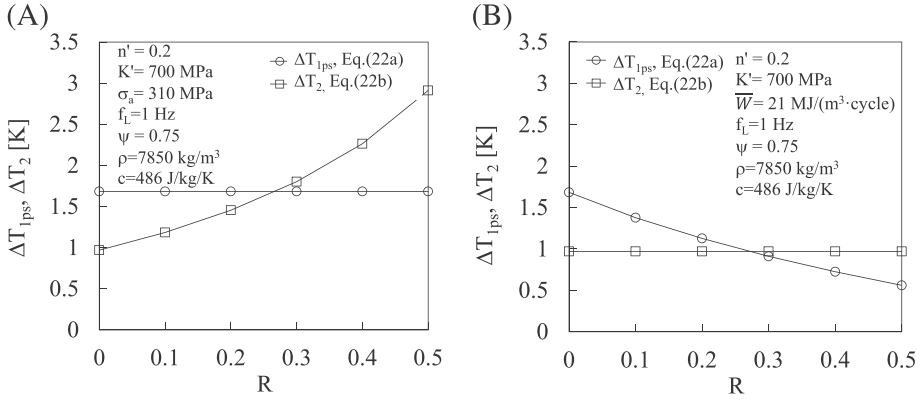

FIGURE 7 ΔT_{1ps} and ΔT_2 versus R evaluated for (A) constant applied stress amplitude and (B) constant plastic strain energy density per cycle $\overline{W}$.

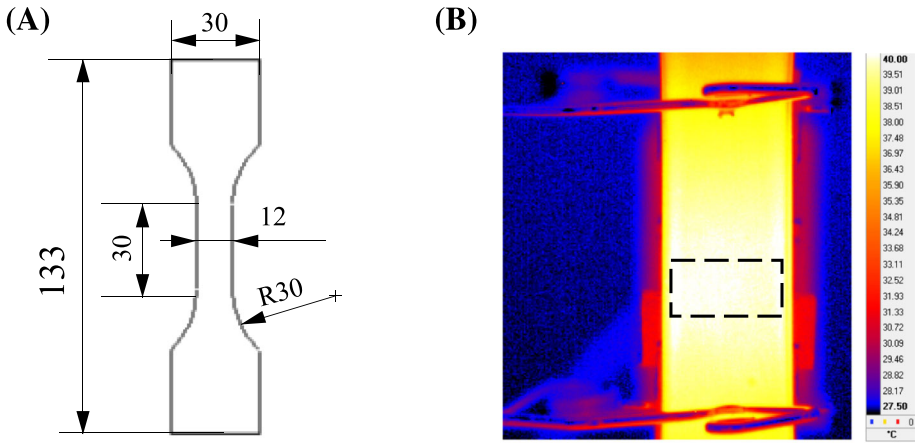

FIGURE 8 (A) Adopted specimen geometry (thickness equal to 6 mm). (B) Acquired temperature map and area considered for evaluating the material temperature ($\sigma_a = 310$ MPa, $f_L = 4.5$ Hz). [Colour figure can be viewed at wileyonlinelibrary.com]

TABLE 1 C45 steel material properties.

σ_Y [MPa]	σ_U [MPa]	E [GPa]	$\sigma_{A,0.1}$ [MPa]	ρ [kg/m^3]	c [J/(kg·K)]	α [K^{-1}]
453	746	207.7	235	7850	486	$12 \cdot 10^{-6}$

6-mm-thick, hot-rolled normalized C45 steel plates, and the material properties are listed in Table 1. The plain material fatigue limit $\sigma_{A,0.1}$ was determined through a short staircase procedure involving seven specimens.

Three specimens were fatigue tested, using a servo-hydraulic Schenck Hydropuls PSA 100 machine equipped with a 100 kN load cell and a TRIO Sistemi RT3 digital controller. Using step-wise fatigue tests for each specimen, a total number of 56 evaluations of the intrinsic dissipation (28 using the second harmonic approach and 28 using the cooling gradient approach) are performed, while in the preliminary investigation[47] with a single specimen only two measurements (one for the second harmonic approach and one for the cooling gradient approach) of the intrinsic dissipation were performed. During the fatigue tests, the applied stress amplitude was progressively increased from 150 to 310 MPa using steps of 20 MPa until specimen's failure, and each step was maintained at least for 5000 cycles to achieve the stabilized material temperature $\overline{T}_s$. At each stress level, the area of the hysteresis loops was calculated from the signals acquired from the load cell and a 25-mm-gauge length MTS extensometer.

The load test frequency f_L was kept in the range 4–10 Hz depending on the applied stress amplitude, and the maximum acceptable stabilized temperature $\overline{T}_s$ was set to 60°C. More precisely, for applied stress amplitudes between 150 and 210 MPa, the load test frequency was set to $f = 10$ Hz, and the observed hysteresis energy density per cycle was practically null ($\overline{W}_{hyst} \cong 0$). For applied stress amplitudes greater than 230 MPa, the load test frequency was kept in the range 4–7 Hz, and it was progressively reduced with the increasing applied stress amplitude to compensate for the progressively stronger self-heating of the material. However, the applicable load test frequency was not limited by an excessive temperature increase approaching the upper limit of 60°C but by the maximum sampling frequency of the adopted infrared camera, which had to return an appropriate amount of temperature data per fatigue cycle to reliably evaluate the temperature harmonics. Only during the last load step before the specimen's fatigue failure did the excessive temperature increase force a limitation of the load test frequency. In fact the high applied load amplitude caused a rapid increase of the temperature towards the upper limit of 60°C, which had to be compensated by a reduction of the load test frequency to typical values of 4–5 Hz.

After grinding with emery paper grade 800 and cleaning with isopropyl alcohol, the specimen surface was painted with matte black paint for uniformity and emissivity enhancement. The material temperature was measured using a FLIR SC7600 infrared camera with the ALTAIR 5.90.002 commercial software by setting the sampling frequency of the temperature data $f_{acq} = 204.8$ Hz. According to the adopted load test frequencies, the lowest number of temperature data points per fatigue cycle was $204.8/10 \cong 20$ data points per fatigue cycle. During the fatigue tests, the spatial resolution was 0.14 mm/px.

To comparatively evaluate the $\overline{Q}_p$ values according to the cooling gradient (Equation (6)) and the second harmonic (Equation (9)) approaches, two sequential temperature acquisitions were performed, both consisting of a 40-s long sampling window: the first acquisition was executed during the running test and captured the stationary

material temperature, while the second acquisition was performed immediately after stopping the test at $t = t^*$ (Figure 1) to capture the cooling gradient.

Regarding the temperature data recorded during the running test (the first acquisition), the FLIR MotionByInterpolation tool was first run to compensate for the relative motion between the fixed infrared camera and the oscillating specimen under the fatigue test. Then, the average temperature of the area where the material temperature was the highest was extracted from the motion-compensated video, as illustrated in Figure 8B. The focus area was placed along the specimen's length to obtain the maximum temperature signal emitted by the specimen, and its size was chosen to be as large as possible to reduce the noise and increase the signal-to-noise ratio. However, the size of the chosen area was ineffective in the resulting second-harmonic temperature range. In fact, ΔT_2 is related to plastic dissipation effects, which are uniformly distributed in the gauge length of the specimen since the stress is also uniform and the material is supposed to be homogeneous.

After extracting from the focus area the vector of average temperature data, the ranges of the first (ΔT_1) and second (ΔT_2) harmonics (defined analytically by Equations (22a) and (22b)) were evaluated numerically using the DFT calculated with the dedicated fast Fourier transform (FFT) routine of MATLAB 2021 commercial software.

The DFT formulae corresponding to the Fourier series Equations (20–22) are as follows:

$$T_r = \overline{T}_s + \sum_{j=1}^{n_{acq}} \left[A_j \cdot \cos\left(\frac{2\pi}{n_{acq}} \cdot r \cdot j\right) + B_j \cdot \sin\left(\frac{2\pi}{n_{acq}} \cdot r \cdot j\right) \right] \tag{28}$$

$$A_j = \frac{2}{n_{acq}} \cdot \sum_{i=0}^{n_{acq}-1} T_i \cdot \cos\left(\frac{2\pi}{n_{acq}} \cdot i \cdot j\right) \text{ for } j > 1 \tag{29a}$$

$$B_j = \frac{2}{n_{acq}} \cdot \sum_{i=0}^{n_{acq}-1} T_i \cdot \sin\left(\frac{2\pi}{n_{acq}} \cdot i \cdot j\right) \text{ for } j \geq 0 \tag{29b}$$

$$\overline{T}_s = \frac{A_0}{2} = \frac{1}{n_{acq}} \cdot \sum_{i=0}^{n_{acq}-1} T_i \tag{29c}$$

$$\Delta T_j = 2 \cdot \sqrt{A_j{}^2 + B_j{}^2} \tag{29d}$$

$$\Delta T_1 = 2 \cdot \sqrt{A_{j^*}{}^2 + B_{j^*}{}^2} \tag{29e}$$

$$\Delta T_2 = 2 \cdot \sqrt{A_{j^{**}}{}^2 + B_{j^{**}}{}^2} \tag{29f}$$

where j* and j** are the j-indices relevant to the first and second harmonics, respectively. A challenge emerged while evaluating the second-harmonic temperature when the closed-loop controller of the testing machine added high-order harmonics to the fundamental (first-order, pure sinusoidal) command signal. The presence of high-order harmonics could be easily assessed by performing a harmonic analysis of the load signal measured by the load cell. Evidently, the second harmonic contribution of the testing machine had to be removed; otherwise, the second-harmonic temperature could not be interpreted as the intrinsic dissipation temperature.

The procedure to clean the second harmonic of the testing machine is as follows. The DFT of the applied stress is simply evaluated by dividing the load cell signal by the specimen's cross-sectional area A. The relevant expressions corresponding to Equations (28–29) are as follows:

$$\sigma_r = \sigma_m + \sum_{j=1}^{n_{acq}} \left[A_{\sigma,j} \cdot \cos\left(\frac{2\pi}{n_{acq}} \cdot r \cdot j\right) + B_{\sigma,j} \cdot \sin\left(\frac{2\pi}{n_{acq}} \cdot r \cdot j\right) \right] \tag{30}$$

$$A_{\sigma,j} = \frac{2}{n_{acq}} \cdot \sum_{i=0}^{n_{acq}-1} \frac{F_i}{A} \cdot \cos\left(\frac{2\pi}{n_{acq}} \cdot i \cdot j\right) \text{ for } j > 1 \tag{31a}$$

$$B_{\sigma,j} = \frac{2}{n_{acq}} \cdot \sum_{i=0}^{n_{acq}-1} \frac{F_i}{A} \cdot \sin\left(\frac{2\pi}{n_{acq}} \cdot i \cdot j\right) \text{ for } j \geq 0 \tag{31b}$$

$$\sigma_m = \frac{A_{\sigma,0}}{2} = \frac{1}{n_{acq}} \cdot \sum_{i=0}^{n_{acq}-1} \frac{F_i}{A} \tag{31c}$$

$$\Delta\sigma_1 = 2 \cdot \sqrt{A_{\sigma,j^*}{}^2 + B_{\sigma,j^*}{}^2} \tag{31d}$$

$$\Delta\sigma_2 = 2 \cdot \sqrt{A_{\sigma,j^{**}}{}^2 + B_{\sigma,j^{**}}{}^2} \tag{31e}$$

where F_i is the sampled force data and $(A_{\sigma,j^*}, B_{\sigma,j^*})$ and $(A_{\sigma,j^{**}}, B_{\sigma,j^{**}})$ are the coefficients relevant to the first and the second harmonics of the applied stress signal, respectively. Then, the corrected range ΔT_2^* of the second-harmonic temperature to exclude the second-order harmonic of the test machine is calculated from Equation (29f):

$$\Delta T_2^* = 2\sqrt{\left(A_{j^{**}} - A_{\sigma,j^{**},the}\right)^2 + \left(B_{j^{**}} - B_{\sigma,j^{**},the}\right)^2} \tag{32}$$

where $A_{\sigma,j^{**},the}$ and $B_{\sigma,j^{**},the}$ are evaluated according to Equation (15):

$$A_{\sigma,j^{**},the} = -\left(\frac{\alpha}{\rho c}\right) T_o \cdot A_{\sigma,j^{**}} \tag{33a}$$

$$B_{\sigma,j^{**},the} = -\left(\frac{\alpha}{\rho c}\right) T_o \cdot B_{\sigma,j^{**}} \tag{33b}$$

Compared to the approach adopted in the previous investigation,[47] the new equations (Equation (33)) exclude the undesired contribution of the second harmonic generated by the closed-loop digital controller using a more consistent mathematical approach because the odd and even coefficients of the second-harmonic temperature signal are corrected individually.

The material of the present paper was investigated previously[49]; for $R = -1$, the $\Delta\sigma_1/\Delta\sigma_2$ ratio varied starting from 250 to 120 for progressively increasing stress ranges during the stepwise fatigue tests, whereas for $R = 0.1$ of the present investigation, a significantly lower ratio is evaluated, namely in the range 100–28, as shown in the next section. Therefore, for $R = -1$, $\Delta T_2^* \cong \Delta T_2$, suggesting that the second-harmonic temperature signal did not need to be cleaned from the second harmonic of the testing machine; conversely, $\Delta T_2^* \neq \Delta T_2$ for $R = 0.1$ when considering the laboratory test conditions of the present investigation, as noted by Cappello et al.,[49] and therefore, ΔT_2^* is to be adopted in Equation (9) instead of ΔT_2. To conclude this section, the procedure to apply the second harmonic approach is summarized in Figure 9.

5 | EXPERIMENTAL RESULTS

Figure 10 shows the characteristic hysteresis loops measured during the fatigue tests for different applied stress amplitudes, σ_a. In general, for stress amplitudes lower than 230 MPa (below the plain material fatigue limit, Table 1), the area enclosed by the hysteresis loops is negligibly small; in the same figure, some hysteresis loops are enlarged to highlight their shapes. Moreover, a typical strain ratcheting is observed, as found in tension–tension fatigue of C45 steel.[7,44,61–63]

After setting the reference coordinate system at the lower tips of the hysteresis loops, the K′ and n′ material parameters are evaluated by individually best fitting the loading branch of the measured hysteresis loop at each load step according to the Ramberg–Osgood equation:

$$\Delta\varepsilon^*(t) = \frac{\Delta\sigma^*(t)}{E} + 2\left(\frac{\Delta\sigma^*(t)}{2 \cdot K'}\right)^{1/n'} \tag{34}$$

In Equation (34), the elastic modulus E was calculated by fitting the increasing and decreasing linear parts of the hysteresis loop.[64] As an example, Figure 11A shows

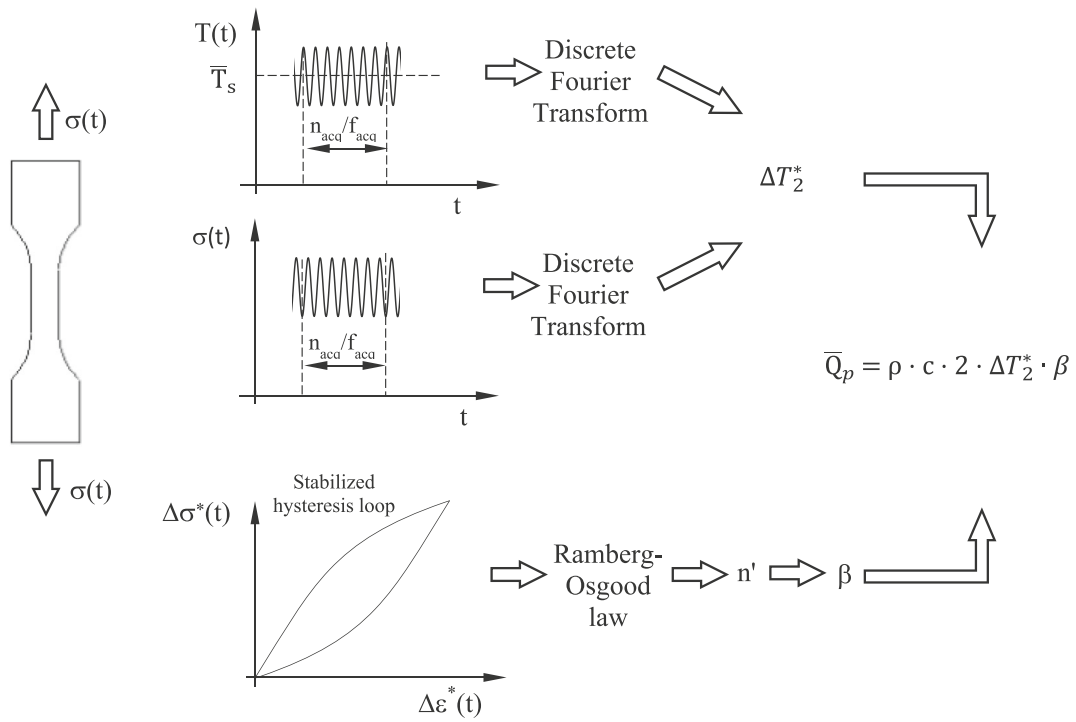

FIGURE 9 Workflow to apply the second harmonic approach.

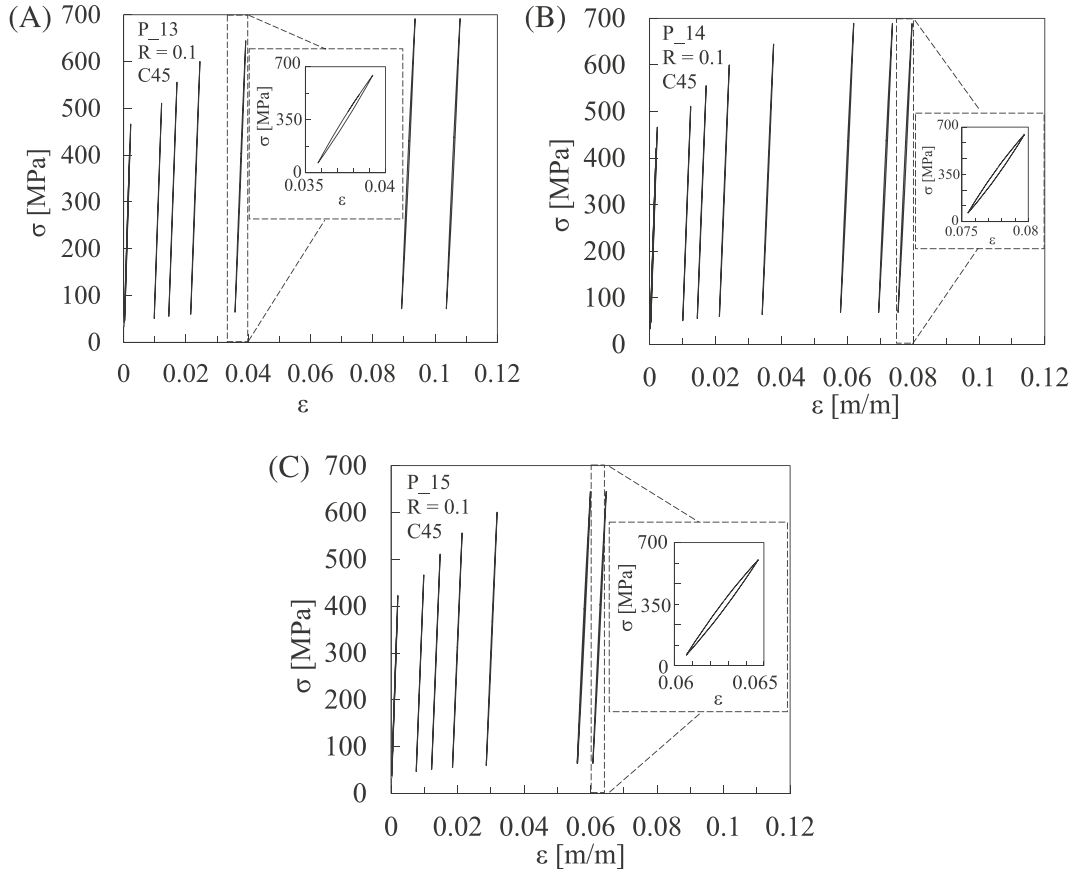

FIGURE 10 Hysteresis loops measured during the stepwise tension–tension fatigue tests on normalized C45 carbon steel for (A) P_13, (B) P_14, and (C) P_15 specimens.

the stabilized hysteresis loops for the P_14 specimen, which clearly exhibit a non-Masing behavior. The typical fitting obtained in the stepwise fatigue tests is plotted in Figure 11B,C for $\sigma_a = 250$ MPa and $\sigma_a = 310$ MPa, respectively; in general, the experimental data are very consistent with Equation (34), regardless of the applied stress amplitude, and almost identical slopes of the decreasing and increasing linear parts of the hysteresis loop are noted. After evaluating the n' values, β is evaluated according to Equation (23), which returns $\beta = 2.818$ and $\beta = 2.750$ for $\sigma_a = 250$ MPa and $\sigma_a = 310$ MPa, respectively.

The results of the DFT of the stationary material temperature measured for the P_14 specimen are reported in Figure 12A,C for $\sigma_a = 250$ MPa, $f_L = 7$ Hz and $\sigma_a = 310$ MPa, $f_L = 4.5$ Hz, respectively. Regarding $\sigma_a = 250$ MPa, Equation (29e) returns $\Delta T_1 = 46.8 \cdot 10^{-2}$ K, and Equation (29f) returns $\Delta T_2 = 1.10 \cdot 10^{-2}$ K, whereas for $\sigma_a = 310$ MPa, the results are $\Delta T_1 = 63.5 \cdot 10^{-2}$ K and $\Delta T_2 = 3.06 \cdot 10^{-2}$ K. Notably, ΔT_2 is on the order of hundredths of a Kelvin and is therefore close to the accuracy of the adopted infrared camera (noise equivalent temperature difference [NETD] < 25 mK and an overall accuracy of 0.05 K[46]). The reduced values of ΔT_2 compared to the overall accuracy of the adopted infrared camera are attributed to different reasons, namely, (i) the limited hysteresis energy density per cycle $\overline{W}_{hyst}$ which translates into reduced ΔT_2 values according to the formulae (27), (8), and (9) applied in sequence, (ii) the spreading of the intrinsic dissipation into all harmonics of the temperature signal such that the second-harmonic temperature ΔT_2 contains only a fraction of the complete information, and (iii) the small fraction of the plastic strain energy density per cycle, $\overline{W}$, converted to intrinsic dissipation in the tension–tension fatigue, differently from the tension–compression fatigue, as will be commented later. Reduced values of ΔT_2 are reported also in the literature.[7,44,49] Figure 12B,D shows the DFT of the load cell signal of the testing machine and demonstrates the presence of high-order harmonics with that modulated at the fundamental frequency of the applied load.[49] In particular, $\Delta\sigma_1/\Delta\sigma_2 = 51.1$ for $\sigma_a = 250$ MPa and $\Delta\sigma_1/\Delta\sigma_2 = 32$ for $\sigma_a = 310$ MPa. By cleaning the range of the second harmonic according to Equation (32), the corrected values result in $\Delta T_2^* = 1.43 \cdot 10^{-3}$ K for $\sigma_a = 250$ MPa and

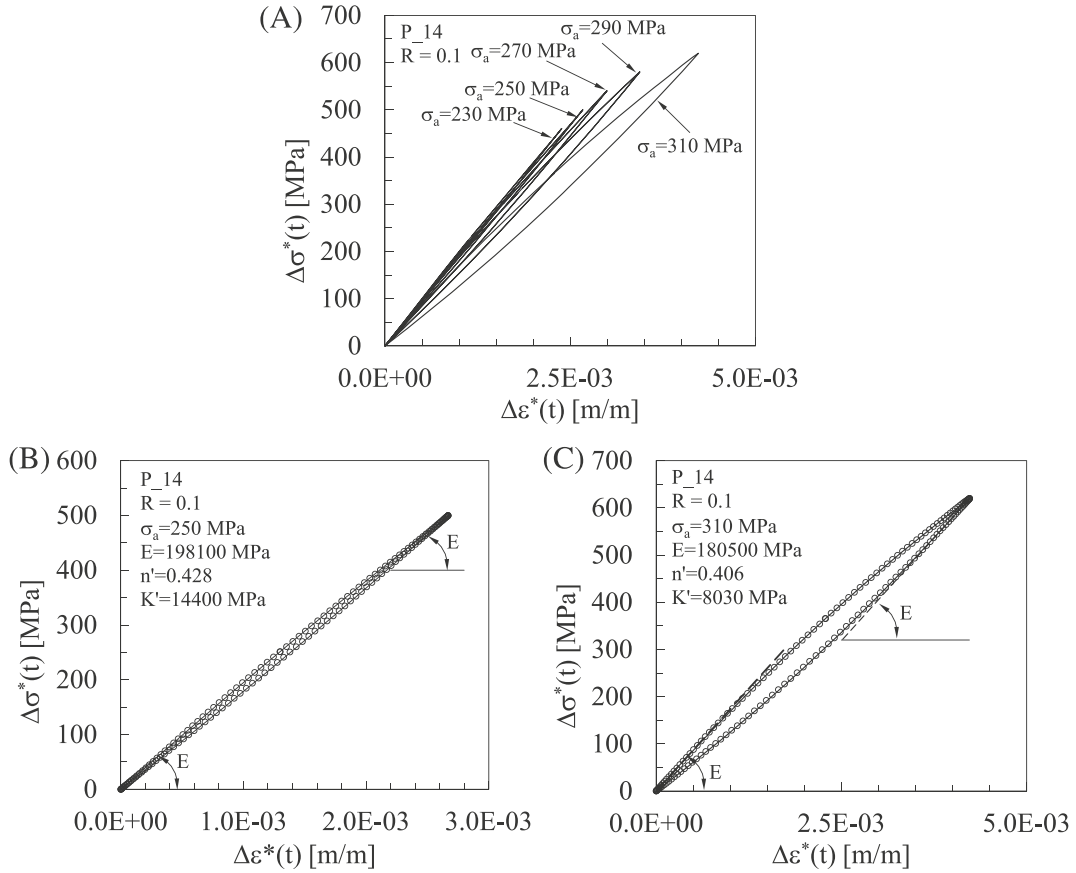

FIGURE 11 Examples of (A) hysteresis loops (P_14 specimen) and fitted Ramberg–Osgood parameters Equation (34) for (B) $\sigma_a = 250$ MPa and (C) $\sigma_a = 310$ MPa.

$\Delta T_2^* = 1.10 \cdot 10^{-2}$ K for $\sigma_a = 310$ MPa. The horizontal axis of Figure 12 reports the discrete frequencies f_j ($f_j = j \cdot f_{acq}/n_{acq}$), and the maximum value of the vertical axis is chosen to greatly emphasize the ranges of the second harmonic (ΔT_2 and $\Delta\sigma_2$); as a consequence, the $\overline{T}_s$ (Equation (29c)) and σ_m (Equation (31c)) values are out of scale. According to the second harmonic approach (Equation (9)), the intrinsic dissipation results in $\overline{Q}_{p,2^{nd}\,harmonic} = 3.08 \cdot 10^{-2}$ MJ/(m^3 cycle) for $\sigma_a = 250$ MPa and $\overline{Q}_{p,2^{nd}\,harmonic} = 2.31 \cdot 10^{-1}$ MJ/(m^3 cycle) for $\sigma_a = 310$ MPa.

These values can be compared with the corresponding estimations using the cooling gradient approach. Figure 13 shows the cooling gradients measured after the test stopped at $t = t^*$ (Figure 1) for $\sigma_a = 250$ MPa, $f_L = 7$ Hz (Figure 13A, $\dot{T}\big|_{t=(t*)^+} = -9.80 \cdot 10^{-2}$ K/s) and $\sigma_a = 310$ MPa, $f_L = 4.5$ Hz (Figure 13B, $\dot{T}\big|_{t=(t*)^+} = -0.251$ K/s). The adopted time window for evaluating the cooling gradients is on the order of 2 s, where the cooling gradient is practically constant, and the corresponding temperature variation is on the order of 2 tenths and 5 tenths of a Kelvin for $\sigma_a = 250$ MPa and $\sigma_a = 310$ MPa, respectively, which is one order of magnitude higher than ΔT_2. Therefore, the signal-to-noise ratio is more favorable in the cooling gradient approach than in the second harmonic approach, as discussed later. Similar results were reported in Meneghetti and Ricotta[46] regarding stepwise tension–compression fatigue tests on AISI 304L cold-drawn bars. Finally, by applying Equation (9), the intrinsic dissipation according to the cooling gradient approach is found to be $\overline{Q}_{p,cooling} = 5.34 \cdot 10^{-2}$ MJ/(m^3 cycle) for $\sigma_a = 250$ MPa and $\overline{Q}_{p,cooling} = 2.13 \cdot 10^{-1}$ MJ/(m^3 cycle) for $\sigma_a = 310$ MPa.

Figure 14A–C collects all available data and compares the intrinsic dissipation $\overline{Q}_p$ calculated following the second harmonic approach (Equations (9) and (23)) and cooling gradient approach (Equation (6)). The percentage difference, e% ($e\% = \left[\left(\left|\overline{Q}_{p,2^{nd}\,harmonic} - \overline{Q}_{p,cooling}\right|\right)/\overline{Q}_{p,cooling}\right] \cdot 100$), between the two approaches is plotted on the secondary y-axis of Figure 14A–C and shows that they are more consistent with each other as the applied stress amplitudes increase, which is attributed to the favorable signal-to-noise ratio of the temperature signals.

After calculating $\overline{W}$ according to Equation (25) and evaluating $\overline{Q}_p$ according to the cooling gradient

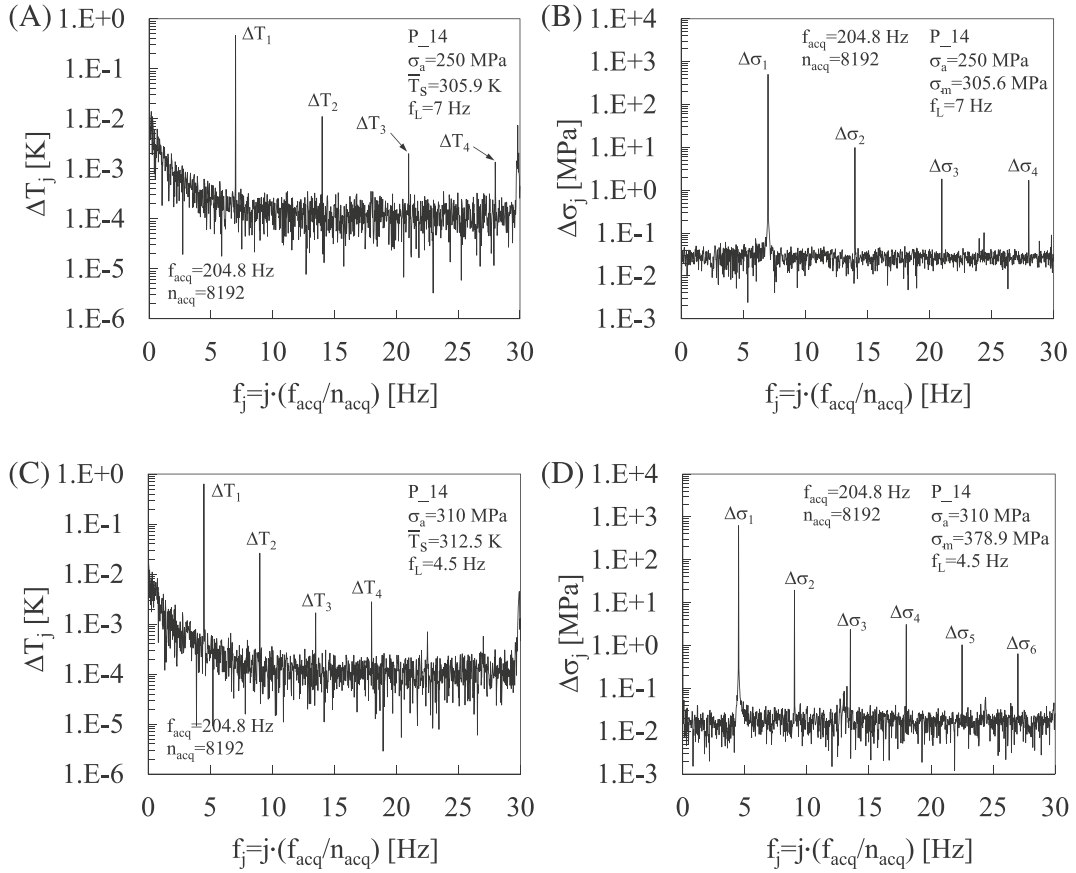

FIGURE 12 Discrete Fourier transform (DFT) of the (A), (C) temperature and of the (B), (D) load cell signals measured for the P_14 specimen tested at (A), (B) $\sigma_a = 250$ MPa and (C), (D) $\sigma_a = 310$ MPa.

approach, the energy conversion ratio averaged over one loading cycle $\overline{\Psi}$ is calculated, and the results are reported in Figure 14D. Although the evaluated data are affected by a certain level of scatter, the trend is that $\overline{\Psi}$ decreases as the applied stress amplitude increases. At the lowest applied stress amplitude of 230 MPa, the energy conversion ratio spans from 0.55 to 0.85, while at the highest applied stress amplitude, it is between 0.37 and 0.45. Notably, such values relevant to tension–tension fatigue with $R = 0.1$ are significantly lower than $\overline{\Psi} \cong 1$, which was found in several investigations with fully reversed ($R = -1$) axial fatigue tests.[27,31,58]

6 | DISCUSSION

In this paper, the intrinsic dissipation $\overline{Q}_p$ is evaluated in tension–tension fatigue tests. Two approaches are used: the second harmonic approach, which takes the Fourier analysis of the material temperature as the starting point, and the cooling gradient approach, which was formalized previously[25] and takes as the starting point the cooling gradient of the material immediately after the fatigue test stops. Both approaches are based on classical continuum mechanics under the hypothesis that the material is homogeneous, but they follow different tracks.

The second harmonic approach is based on Equation (9), where the β coefficient relates the second-harmonic temperature to the intrinsic dissipation; β is evaluated theoretically by analyzing a virtual experiment and solving the governing energy balance Equation (1). The virtual experiment consists of a zero-dimensional thermomechanical problem where an elastic–plastic material obeying the Ramberg–Osgood law is subjected to uniform stress and temperature fields. To simulate the intrinsic dissipation causing self-heating of the material, a coefficient capturing the energy conversion ratio is introduced (Equation (8)). To achieve stationarity of the time-dependent material temperature, the virtual experiment simulates heat extraction from the material using a simple heat sink. Considering the stationary, periodic material temperature, Fourier analysis is performed, and the range of the second-harmonic temperature signal (Equation (22b)) is evaluated. Then Equation (9) returns the intrinsic dissipation, where β is evaluated

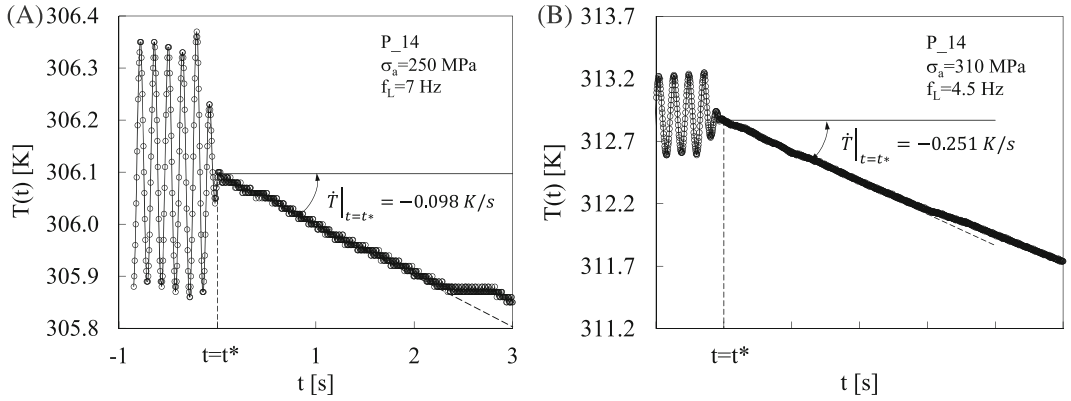

FIGURE 13 Examples of cooling gradient (P_14 specimen) for (A) $\sigma_a = 250$ MPa and (B) $\sigma_a = 310$ MPa.

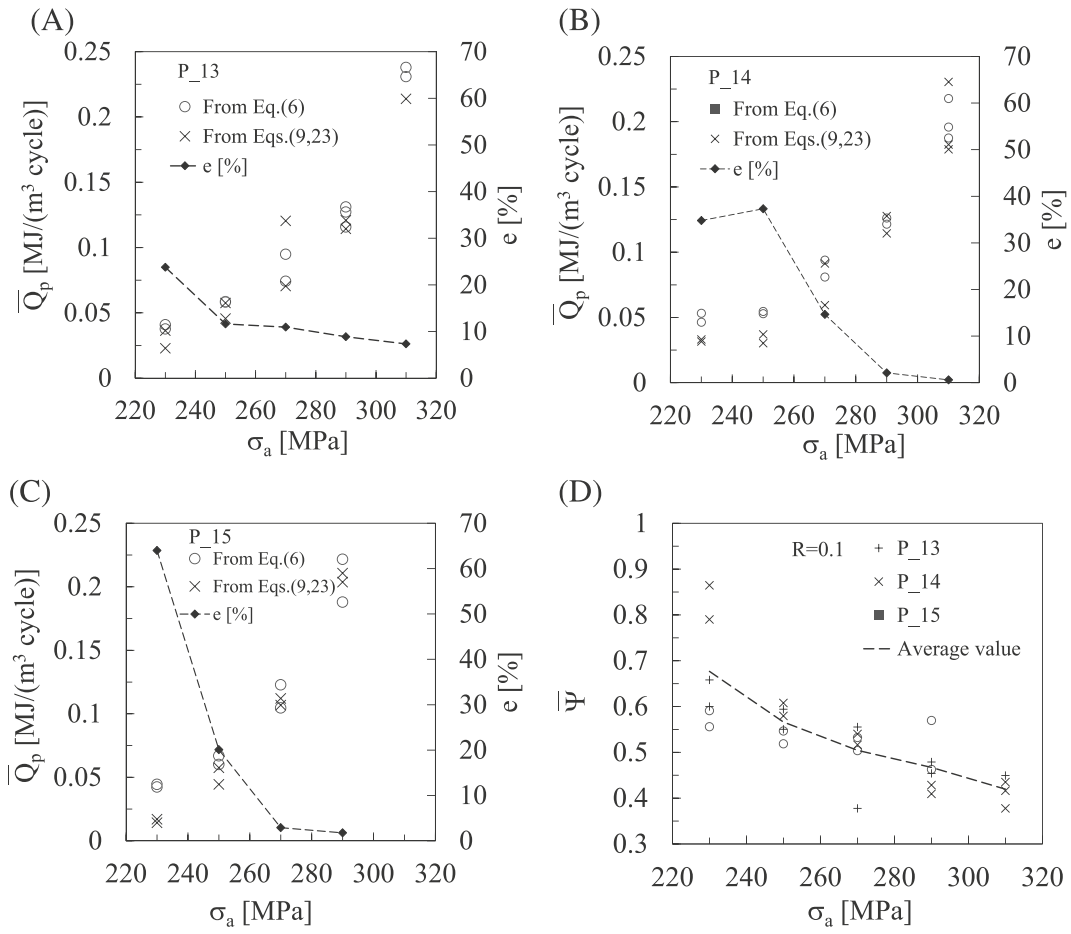

FIGURE 14 Comparison between the intrinsic dissipation $\overline{Q}_p$ according to the cooling gradient approach (Equation (6)) and the second harmonic approach (Equations (9) and (23)) for (A) P_13, (B) P_14, and (C) P_15 specimens. (D) Energy conversion ratio $\overline{\Psi}$ measured during the R = 0.1 stepwise fatigue tests.

with Equation (23) for load ratios $R \geq 0$, as a function of the cyclic strain hardening exponent n′ of the material. A different expression is true for $R = -1$.[45] The coefficient β depends on the thermal boundary conditions of the tests and specifically on the adopted model of the heat sink; however, dedicated theoretical and numerical investigations have been conducted previously by heavily perturbating the thermal boundary conditions and β resulted quite independent on them for practical applications.[45,46]

To apply the second harmonic approach, the load test frequency f_L cannot be increased above a certain value because of the maximum sampling rate of the adopted infrared camera; in the present investigation, at least 20 temperature data points per fatigue cycle are measured in view of the subsequent harmonic analysis according to the DFT. Moreover, a challenge is highlighted in the present investigation in that care must be taken due to the potential presence of high-order harmonics produced by the closed-loop feedback control of the fatigue test machine.

Compared to the second harmonic approach, the cooling gradient approach does not need the formalization of any hypothesis regarding the elastic–plastic constitutive law of the material because it only requires the material density and specific heat and is independent of the thermal boundary conditions.[28] On the other hand, the second harmonic approach has the advantage that stopping the test is unnecessary because it relies on temperature acquisitions performed during the running fatigue test. The cooling gradient approach can be applied in a clear manner to evaluate the intrinsic dissipation at the tips of rounded stress concentrators,[25,30] even though the application to severe stress raisers implies some experimental difficulties discussed elsewhere.[28,30] Notably, another practical limitation of the cooling gradient approach emerges when the stabilized temperature $\overline{T}_s$ is close to room temperature, such as when self-heating of the material decreases because of the thermal and mechanical boundary conditions of the tests. Similarly, a reduced intrinsic dissipation adversely affects the application of the second harmonic approach, as can be realized by considering the reduced magnitude of ΔT_2 in the present and previous investigations, which range from a few thousandths to a few hundredths of a Kelvin.[46] To mitigate this limitation, the use of controlled laboratory test conditions and/or a material testing climate chamber can be useful.[40]

7 | CONCLUSIONS

In this paper, the link between the second-harmonic temperature signal and the intrinsic dissipation per cycle (the $\overline{Q}_p$ parameter) of a metal under tension–tension fatigue is investigated, taking advantage of the self-heating phenomenon observed in fatigue tests. Self-heating caused by intrinsic dissipation does not produce a pure sinusoidal wave of temperature, but its effect spreads out into all harmonics of the material temperature as determined through Fourier analysis, starting from the fundamental harmonic modulated at the applied load test frequency. If the load-controlled fatigue test is driven by a pure sinusoidal command signal, the second harmonic (modulated at twice the load test frequency) retains most, but not all, of the information regarding intrinsic dissipation; the first harmonic (modulated at the load test frequency) contains all, but not exclusively, the thermoelastic effect information. If the command signal generated by the closed-loop digital controller of the fatigue test machine contains high-order harmonics, the thermoelastic effect is spread out into high-order harmonics of the material temperature; in this context, the second harmonic approach is developed to clean (if necessary) the second-harmonic temperature signal from the contribution coming from the second harmonic of the command signal. Through a zero-dimensional thermomechanical material model obeying a Ramberg–Osgood law, a coefficient β is determined, which relates the range of the second-harmonic temperature with the intrinsic dissipation per cycle and depends only on the cyclic strain hardening exponent of the material. In the present investigation, the second harmonic approach is experimentally validated using step-load fatigue tests on plain specimens prepared from normalized C45 carbon steel plates. For validation purposes, the intrinsic dissipation calculated using the second harmonic approach is compared to that evaluated according to a well-established approach that was previously published by the authors (the cooling gradient approach). The agreement between the two approaches increases with increasing applied stress amplitudes, which is attributed to the favorable signal-to-noise ratio of the temperature signals. The second harmonic approach benefits more from the improvement of the signal-to-noise ratio than the cooling gradient approach, since the thermal quantities treated in the former method are much lower than those in the latter. Finally, the energy conversion ratio, namely, the ratio between the intrinsic dissipation and the plastic strain energy density per cycle, is evaluated, resulting in a range of 0.55–0.85 at low stress levels and 0.37–0.45 at high stress amplitudes, with reference to the material and test conditions analyzed in the present investigation.

NOMENCLATURE

A_j, B_j	coefficients of the DFT of the temperature signal [K]
A_k, B_k	coefficients of the Fourier series of the temperature signal [K]
$A_{\sigma,j^{**},the}$, $B_{\sigma,j^{**},the}$	thermoelastic second-harmonic coefficients of the DFT of the load signal [K]
$A_{\sigma,j}$, $B_{\sigma,j}$	coefficients of the DFT of the stress signal [MPa]
c	specific heat of the material [J/(kg·K)]
DFT	discrete Fourier transform

E	material elastic modulus [MPa]
$\dot{E}_s$	stored energy rate [W/m^3]
F_i	sampled force data [N]
f_{acq}	sampling rate of the infrared camera [Hz]
f_L	load test frequency [Hz]
K'	cyclic strength coefficient of the material [MPa]
n'	cyclic strain hardening exponent of the material
n_{acq}	number of frames acquired by the infrared camera
$\dot{Q}$	thermal energy rate exchanged by a unit volume of material by conduction, convention, and radiation [W/m^3]
$\overline{Q}$	thermal energy exchanged by a unit volume of material per cycle by conduction, convection, and radiation [J/(m^3·cycle)]
$\overline{Q}_p$	intrinsic dissipation per unit volume of material per cycle (Q_p averaged over one loading cycle) [J/(m^3·cycle)]
$\dot{Q}_{the}$	thermoelastic energy rate per unit volume [W/m^3]
R	nominal stress ratio (ratio between the minimum and the maximum applied nominal stress)
t^*	time at which the fatigue test suddenly stops [s]
T	material temperature [K]
T_i	sampled temperature data [K]
T_p	dissipation temperature (i.e., material temperature related to the intrinsic dissipation) [K]
T_{ps}	stationary dissipation temperature [K]
$\overline{T}_s$	stabilized material temperature (stationary material temperature averaged over one loading cycle) [K]
T_{sink}	temperature associated with the heat sink $\dot{v}_e$ [K]
$\overline{T}_{ps}$	stabilized dissipation temperature (stationary dissipation temperature averaged over one loading cycle) [K]
T_{the}	material temperature related to the thermoelasticity or thermoelastic temperature [K]
$\dot{v}_e$	thermal energy rate per unit volume supplied to or extracted from the material by external sources [W/m^3]
$\dot{W}$	plastic strain energy rate per unit volume of material [W/m^3]
$\overline{W}$	plastic strain energy density per cycle [J/(m^3·cycle)]
$\overline{W}_{hyst}$	hysteresis energy density per cycle (i.e., area of the hysteresis loop) [J/(m^3·cycle)]
α	isotropic coefficient of thermal expansion [K^{-1}]
β	parameter correlating the intrinsic dissipation and the second-harmonic temperature signal [/]
ρ	material density [kg/m^3]
$\sigma(t)$, σ_a, σ_m, σ_{min}	applied stress function, its amplitude, mean value, minimum value, respectively [MPa]
σ_Y	yield strength [MPa]
σ_U	ultimate tensile strength [MPa]
$\sigma_{A,0.1}$	material fatigue limit for load ratio equal to R = 0.1 [MPa]
ΔT_1	range of the first-harmonic temperature [K]
ΔT_2	range of the second-harmonic temperature [K]
ΔT_2^*	corrected range of the second-harmonic temperature to exclude the second-order harmonic of the test machine [K]
ΔT_{1ps}	range of the first-harmonic dissipation temperature (first harmonic of T_{ps}) [K]
ΔT_{2ps}	range of the second-harmonic dissipation temperature (second harmonic of T_{ps}) [K]
$\Delta T_p(t)$	dissipation temperature, evaluated with respect to the $\Delta\sigma^*$–$\Delta\varepsilon^*$ reference system [K]
$\Delta T_{the}(t)$	thermoelastic temperature, evaluated with respect to the $\Delta\sigma^*$–$\Delta\varepsilon^*$ reference system [K]
$\Delta\varepsilon^*(t)$	strain function, evaluated from the lower tip of the hysteresis loop [m/m]
$\Delta\sigma^*(t)$	applied stress function, evaluated from the lower tip of the hysteresis loop [MPa]
$\Delta\sigma_1$	range of the first-harmonic stress [MPa]
$\Delta\sigma_2$	range of the second-harmonic stress [MPa]
Ψ, $\overline{\Psi}$	energy conversion ratio ($\Psi = \dot{Q}_p/\dot{W}$) and its average value over one loading cycle, respectively [/]
ω_L	angular frequency of the applied stress ($\omega_L = 2\cdot\pi\cdot f_L$) [rad/s]

ACKNOWLEDGMENTS

This work was co-funded by the European Union (grant agreement no. 101058179; ENGINE). However, the views and opinions expressed are those of only the authors and do not necessarily reflect those of the

European Union or the European Health and Digital Executive Agency. Neither the European Union nor the granting authority can be held responsible for these opinions.

DATA AVAILABILITY STATEMENT

The data that support the findings of this study are available from the corresponding author upon reasonable request.

ORCID

Mauro Ricotta https://orcid.org/0000-0002-3517-9464
Giovanni Meneghetti https://orcid.org/0000-0002-4212-2618

REFERENCES

1. Ellyin F. *Fatigue Damage, Crack Growth and Life Prediction*. Chapman & Hall; 1997.
2. Dengel D, Harig H. Estimation of the fatigue limit by progressively-increasing load tests. *Fatigue Fract Eng Mater Struct*. 1980;3(2):113-128.
3. Curti G, Geraci AL, Risitano A. A new method for rapid determination of the fatigue limit. *Ingegneria Automotoristica*. 1989; 42:634-636. in italian. doi:10.1007/978-94-009-1509-1
4. Luong MP. Fatigue limit evaluation of metals using an infrared thermographic technique. *Mech Mater*. 1998;28(1-4):155-163.
5. La Rosa G, Risitano A. Thermographic methodology for rapid determination of the fatigue limit of materials and mechanical components. *Int J Fatigue*. 2000;22(1):65-73. doi:10.1016/S0142-1123(99)00088-2
6. Huang J, Pastor ML, Garnier C, Gong X. Rapid evaluation of fatigue limit on thermographic data analysis. *Int J Fatigue*. 2017;104:293-301.
7. Colombo C, Sansone M, Patriarca L, Vergani L. Rapid estimation of fatigue limit for C45 steel by thermography and digital image correlation. *J Strain Anal Eng des*. 2021;56(7):478-491.
8. Zhao A, Xie J, Zhao Y, et al. Fatigue limit evaluation via infrared thermography for a high strength steel with two strength levels. *Eng Fract Mech*. 2022;268:108460.
9. Ranc N, Palin-Luc T, Paris PC, Saintier N. About the effect of plastic dissipation in heat at the crack tip on the stress intensity factor under cyclic loading. *Int J Fatigue*. 2014;58:56-65.
10. Brooks C, Rajic N. Automated visual tracking of crack growth in coupon and component level fatigue testing using thermoelastic stress analysis. *Int J Fatigue*. 2022;163:107037.
11. Palumbo D, de Finis R, di Carolo F, Vasco-Olmo J, Diaz FA, Galietti U. Influence of second-order effects on thermoelastic behaviour in the proximity of crack tips on titanium. *Exp Mech*. 2022;62(3):521-535. doi:10.1007/s11340-021-00789-4
12. Pitarresi G, Cappello R. Evaluation of crack-closure by second harmonic thermoelastic stress analysis. *Int J Fatigue*. 2022;164: 107116.
13. Bercelli L, Levieil B, Doudard C, Malek B, Bridier F, Ezanno A. Use of infrared thermography to model the effective stress ratio effect on fatigue crack growth in welded T-joints. *Eng Fract Mech*. 2023;279:109061.
14. Ezanno A, Doudard C, Calloch S, Heuzé JL. A new approach to characterizing and modelling the high cycle fatigue properties of cast materials based on self-heating measurements under cyclic loadings. *Int J Fatigue*. 2013;47:232-243. doi:10.1016/j.ijfatigue.2012.09.005
15. Williams P, Liakat M, Khonsari MM, Kabir OM. A thermographic method for remaining fatigue life prediction of welded joints. *Mater Des*. 2013;51:916-923.
16. Zhang L, Liu XS, Wu SH, Ma ZQ, Fang HY. Rapid determination of fatigue life based on temperature evolution. *Int J Fatigue*. 2013;54:1-6.
17. Risitano A, Risitano G. Cumulative damage evaluation of steel using infrared thermography. *Theor Appl Fract Mec*. 2010; 54(2):82-90. doi:10.1016/j.tafmec.2010.10.002
18. Poncelet M, Doudard C, Calloch S, Weber B, Hild F. Probabilistic multiscale models and measurements of self-heating under multi-axial high cycle fatigue. *J Mech Phys Solids*. 2010;58(4): 578-593.
19. Skibicki D, Lipski A, Pejkowski Ł. Evaluation of plastic strain work and multiaxial fatigue life in CuZn37 alloy by means of thermography method and energy-based approaches of Ellyin and Garud. *Fatigue Fract Eng Mater Struct*. 2018;41(12):2541-2556.
20. Feng E, Wang X, Jiang C, Crupi V. Quantitative thermographic method for fatigue life prediction under variable amplitude loading. *Fatigue Fract Eng Mater Struct*. 2022;45(4):1199-1212.
21. Louge J, Moyne S, Doudard C, Calloch S, Weber B, Munier R. Self-heating measurements under cyclic loading to identify history effects on HCF properties of high-strength low-alloy steel: part I—experimental investigations. *Fatigue Fract Eng Mater Struct*. 2023;46(1):171-181.
22. Krapez JC, Pacou D, Gardette G. Lock-in thermography and fatigue limit of metals. In Proceedings of the Q.I.R.T, Reims, France, 18–21 2000.
23. Akai A, Sato Y, Murase M, Kojima Y, Okubo Y. Rapid determination of fatigue limit using temperature second harmonic. *Exp Mech*. 2023;63(2):349-362.
24. De Finis R, Palumbo D, Galietti U. A multianalysis thermography-based approach for fatigue and damage investigations of ASTM A182 F6NM steel at two stress ratios. *Fatigue Fract Eng Mater Struct*. 2019;42(1):267-283.
25. Meneghetti G. Analysis of the fatigue strength of a stainless steel based on the energy dissipation. *Int J Fatigue*. 2007;29(1): 81-94.
26. Meneghetti G, Ricotta M. The heat energy dissipated in the material structural volume to correlate the fatigue crack growth rate in stainless steel specimens. *Int J Fatigue*. 2018;115: 107-119.
27. Meneghetti G, Ricotta M. The use of the specific heat loss to analyse the low- and high cycle fatigue behaviour of plain and notched specimens made of a stainless steel. *Eng Fract Mech*. 2012;81:2-16. doi:10.1016/j.engfracmech.2011.06.010
28. Meneghetti G, Ricotta M, Atzori B. A synthesis of the push-pull fatigue behaviour of plain and notched stainless steel specimens by using the specific heat loss. *Fatigue Fract Eng Mater Struct*. 2013;36(12):1306-1322. doi:10.1111/ffe.12071
29. Meneghetti G, Ricotta M, Negrisolo L, Atzori B. A synthesis of the fatigue behaviour of stainless steel bars under fully reversed axial or torsion loading by using the specific heat loss. *Key Eng*

Mater. 2013;577-578:453-456. doi:10.4028/www.scientific.net/KEM.577-578.453
30. Rigon D, Ricotta M, Meneghetti G. An analysis of the specific heat loss at the tip of severely notched stainless steel specimens to correlate the fatigue strength. *Theor Appl Fract Mech*. 2017;92:240-251.
31. Ricotta M, Meneghetti G, Atzori B, Risitano G, Risitano A. Comparison of experimental thermal methods for fatigue limit evaluation of a stainless steel. *Metals*. 2019;9(6):677-700. doi:10.3390/met9060677
32. Rigon D, Berto F, Meneghetti G. Estimating the multiaxial fatigue behaviour of C45 steel specimens by using the energy dissipation. *Int J Fatigue*. 2021;151:106381.
33. Guo Q, Guo X, Fan J, Syed R, Wu C. An energy method for rapid evaluation of high-cycle fatigue parameters based on intrinsic dissipation. *Int J Fatigue*. 2015;80:136-144.
34. Guo Q, Guo X. Research on high-cycle fatigue behavior of FV520B stainless steel based on intrinsic dissipation. *Mater des*. 2016;90:248-255.
35. Feltner CE, Morrow JD. Microplastic strain hysteresis energy as a criterion for fatigue fracture. *J Basic Eng*. 1961;83(1):15-22. doi:10.1115/1.3658884
36. Halford GR. The energy required for fatigue. *J Mater*. 1966;19:3-18. doi:10.1115/1.3658884
37. Liakat M, Khonsari M. Entropic characterization of metal fatigue with stress concentration. *Int J Fatigue*. 2015;70:223-234. doi:10.1016/j.ijfatigue.2014.09.014
38. Mahmoudi A, Khonsari MM. Investigation of metal fatigue using a coupled entropy-kinetic model. *Int J Fatigue*. 2022;161:106907. doi:10.1016/j.ijfatigue.2022.106907
39. Enke NF. An enhanced theory for thermographic stress analysis of isotropic materials. In: *Stress and Vibration: Recent Developments in Industrial Measurement and Analysis*. Vol.1084. International Society for Optics and Photonics; 1989:84-102.
40. Bar J, Seilnacth L, Urbanek R. Determination of dissipated energies during fatigue tests on copper and AA7475 with infrared thermography. *Proc Struct Integr*. 2019;17:308-315.
41. Bar J, Urbanek R. Determination of dissipated energy in fatigue crack propagation experiments with lock-in thermography. *Fract Struct Integr*. 2019;48:563-570.
42. Akai A, Shiozawa D, Sakagami T. Fatigue limit evaluation for austenitic stainless steel. *J Soc Mat Sci*. 2012;61(12):953-959. doi:10.2472/jsms.61.953
43. Palumbo D, De Finis R, Demelio GP, Galietti U. Damage monitoring in fracture mechanics by evaluation of the heat dissipated in the cyclic plastic zone ahead of the crack tip with thermal measurements. *Eng Fract Mech*. 2017;181:65-76. doi:10.1016/j.engfracmech.2017.06.017
44. De Finis R, Palumbo D, Galietti U. On the relationship between mechanical energy rate and heat dissipated rate during fatigue for a C45 steel depending on stress ratio. *Fatigue Fract Eng Mater Struct*. 2021;44(10):2781-2799. doi:10.1111/ffe.13547
45. Meneghetti G, Ricotta M. Estimating the intrinsic dissipation using the second harmonic of the temperature signal in tension-compression fatigue. Part I: theory. *Fatigue Fract Eng Mater Struct*. 2021;44(8):2168-2185.
46. Meneghetti G, Ricotta M. Estimating the intrinsic dissipation using the second harmonic of the temperature signal in tension-compression fatigue. Part II: experiments. *Fatigue Fract Eng Mater Struct*. 2021;44(8):2153-2167.
47. Ricotta M, Veronese M, Meneghetti G. Estimating the specific heat loss from temperature measurements in tension-tension fatigue: theory and experiments. In: *European Workshop on Structural Health Monitoring: EWSHM 2022 - Volume 2*. Vol.254. Springer International Publishing; 2023:600-609. doi:10.1007/978-3-031-07258-1_61
48. Shiozawa D, Inagawa T, Washio T, Sakagami T. Accuracy improvement in dissipated energy measurement by using phase information. *Meas Sci Technol*. 2017;28(4):044004. doi:10.1088/1361-6501/28/4/044004
49. Cappello D, Meneghetti G, Ricotta M, Pitarresi G. On the correlation of temperature harmonic content with energy dissipation in C45 steel samples under fatigue loading. *Mech Mater*. 2022;168:104271. doi:10.1016/j.mechmat.2022.104271
50. Lemaitre J, Chaboche JL. *Mechanics of Solid Materials*. Cambridge University Press; 1998. doi:10.1016/j.mechmat.2022.104271
51. Kaleta J, Blotny R, Harig H. Energy stored in a specimen under fatigue limit loading conditions. *J Test Eval*. 1990;19:326-333.
52. Mareau C, Favier V, Weber B, Galtier A, Berveiller M. Micromechanical modeling of the interactions between the microstructure and the dissipative deformation mechanisms in steels under cyclic loading. *Int J Plast*. 2012;32-33:106-120.
53. Pandey KN, Chand S. Deformation based temperature rise: a review. *Int J Pres Ves Pip*. 2003;80(10):673-687. doi:10.1016/j.ijpvp.2003.07.001
54. Charkaluk E, Constantinescu A. Dissipation and fatigue damage. Proceedings of the Fifth International Conference on Low Cycle Fatigue LCF 5, September 9-11, 2003.
55. Birol Y. What happens to the energy input during fatigue crack propagation? *Mat Sci Eng A-Struct*. 1988;104:117-124. doi:10.1016/0025-5416(88)90412-0
56. Wan VVC, MacLachlan DW, Dunne FPE. A stored energy criterion for fatigue crack nucleation in polycrystals. *Int J Fatigue*. 2014;68:90-102. doi:10.1016/j.ijfatigue.2014.06.001
57. Yao Y, Wang J, Keer LM. A phase transformation based method to predict fatigue crack nucleation and propagation in metals and alloys. *Acta Mater*. 2017;127:244-251. doi:10.1016/j.actamat.2017.01.039
58. Lu X, Dunne F, Xu Y. A crystal plasticity investigation of slip system interaction, GND density and stored energy in non-proportional fatigue in Nickel-based superalloy. *Int J Fatigue*. 2020;139:105782. doi:10.1016/j.ijfatigue.2020.105782
59. Wong AK, Sparrow JG, Dunn SA. On the revised theory of the thermoelastic effect. *J Phys Chem Solid*. 1988;49(4):395-400. doi:10.1016/0022-3697(88)90099-6
60. Pitarresi G, Patterson EA. A review of the general theory of thermoelastic stress analysis. *J Strain Anal Eng Des*. 2003;38(5):405-417.
61. Mocko W. The influence of stress-controlled tensile fatigue loading on the stress–strain characteristics of AISI 1045 steel. *Mater Des*. 2014;58:145-153. doi:10.1016/j.matdes.2014.02.021

62. Kolasangiani K, Farhangdoost K, Shariati M, Varvani-Farahani A. Ratcheting assessment of notched steel samples subjected to asymmetric loading cycles through coupled kinematic hardening-Neuber rules. *Int J Mech Sci*. 2018;144:24-32.
63. Kolasangiani K, Shariati M, Farhangdoost K, Varvani-Farahani A. Ratcheting progress at notch root of 1045 steel samples over asymmetric loading cycles: experiments and analyses. *Fatigue Fract Eng Mater Struct*. 2018;41(9):1870-1883.
64. ASTM E739-10e1. (2010) Standard practice for statistical analysis of linear or linearized stress-life (S-N) and strain-life (ε-N) fatigue data. ASTM International.

How to cite this article: Ricotta M, Meneghetti G. Estimating the intrinsic dissipation using the second-harmonic temperature signal in the tension–tension fatigue. *Fatigue Fract Eng Mater Struct*. 2023;46(11):4218-4238. doi:10.1111/ffe.14132